Supporting Information

Responsive Structural Adaptability in Ultra-Microporous Frameworks: Guest recognition and Macroscopic Shape Transformations Induced by Spin Transitions within Single Crystals

Yu-Ting Yang,[a,b] Wei Guo,[a] Yu-Xia Li,[d] Zhi-Kun Liu,[d] Yuqiao Chai,[b,*] Xing Li,[a] Bao Li,[c,*] and Jin-Peng Xue[a,*]

[a.] Address here. School of Materials Science and Chemical Engineering, Ningbo University, Ningbo, Zhejiang 315211, China.
[b.] School of Material and Chemical Engineering, Ningbo University of Technology, Ningbo, Zhejiang 315211, China.
[c.] Key Laboratory of Material Chemistry for Energy Conversion and Storage, School of Chemistry and Chemical Engineering, Huazhong University of Science and Technology, Wuhan, Hubei 430074, China
[d.] Key Laboratory of Cluster Science of Ministry of Education, School of Chemistry and Chemical Engineering, Beijing Institute of Technology, Beijing 102488, China

Email: xuejinpeng@nbu.edu.cn (J-P.X.); chaiyuqiao@nbut.edu.cn (Y. Chai); libao@hust.edu.cn9 (B.L.)

Table of Contents

Experimental Procedures

[Fe^{II}(tpe)($NCBH_3$)$_2$]·2C_2Cl_4 (1·2C_2Cl_4). A buffer layer consisting of a C_2Cl_4/CH_3OH mixture (4mL, v/v = 1:1) was slowly added to the tube containing a C_2Cl_4/CH_3OH mixture solution (4mL, v/v = 3:1) with the tpe ligand (3.35 mg, 0.01 mmol). Then a CH_3OH solution (4 mL) of [Fe($NCBH_3$)$_2$] (0.03 mmol) was carefully layered on top of the buffer layer. After 1 week, yellow plate-like crystals were grown (yield: 5.8 mg, ~ 72.4% based on tpe ligand). The amount of C_2Cl_4 molecules in the crystal was directly obtained from the single-crystal X-ray diffraction of **1**·2C_2Cl_4, consistent with the elemental and thermogravimetric analyses. Elemental analysis calcd (%) for $C_{28}H_{22}B_2Cl_8FeN_6$: C 41.77, H, 2.75, N, 10.41; found; C, 41.85, H, 2.76, N, 10.46.

[Fe^{II}(tpe)($NCBH_3$)$_2$]·2.5CH_3OH (1·2.5CH_3OH). In an H-type tube, a 4 mL CH_3OH solution containing tpe ligand (6.7 mg, 0.02 mmol) was placed on one side, while a 5 mL CH_3OH solution of [Fe($NCBH_3$)$_2$] (0.05 mmol) was placed on the opposite side. Pure CH_3OH solution was then carefully added to fill the H-type tube completely. After 3 weeks, bright yellow crystals plate-like crystals were obtained.

Powder X-ray diffraction (PXRD). PXRD data were recorded on a Bruker D8 ADVANCE diffractometer with Cu Kα radiation (λ = 1.5418 Å). All samples were loaded onto a glass sample table featuring a circular groove (diameter ~2 cm, thickness ~1 mm). For the measurement of **1**·2.5CH_3OH, a PVC film was used to cover the crystalline powder, ensuring that they remained wetted by the CH_3OH solution throughout the PXRD testing.

Single-crystal X-ray diffraction (SC-XRD) analyses. SC-XRD analyses of **1**·2C_2Cl_4 and the partially desolvated state form **1**·2.5CH_3OH were performed on a Rigaku Oxford XtaLAB PRO diffractometer equipped with graphite-monochromated Mo Kα radiation (λ = 0.71073 Å). The data of **1**·2C_2Cl_4 were collected at 200 K. The partially desolvated single crystal was obtained from the single crystal of **1**·2.5CH_3OH without encapsulated crystal oil under a dry N_2 flow in situ for half an hour at room temperature and the data of that were collected with one sample at 200 and 301 K, respectively.

The fixing method of the single-crystal sample for recording reversible shape changes. The single-crystal sample, used for recording reversible shape changes (Movie 2 and 3), is affixed to glass wires using AB glue. This AB glue softens at approximately 323 K, rendering it ineffective for securely fixing the samples.

The fully desolvated single crystal was obtained by subjecting the single crystal of **1**·2C_2Cl_4 to in situ heating at 448 K using a Bruker D8 diffraction with graphite monochromator Mo Kα radiation (λ= 0.71073 Å). The data of fully desolvated state **1** were collected at 448 and 298 K, respectively.

All the structures were solved using direct methods and subsequently refined through full-matrix least-squares techniques on F^2 with SHELX program.[1] Non-hydrogen atoms underwent anisotropic refinement, while hydrogen atoms were generated geometrically and refined isotropically.

Magnetic measurement. Magnetic measurements were conducted using a Quantum Design MPMS XL-7 magnetometer, operating within the temperature range of 2–400 K and a sweeping rate of 1 K min^{-1} under a magnetic field of 5000 Oe. For crystalline powders of **1**·2C_2Cl_4, measurements were performed following a temperature cycle of 300–2–300 K. Initially, the crystalline powders were heated in a vacuum oven at 500 K for one hour, then enveloped in plastic film and secured within a straw. Subsequent heating at 395 K for one hour in the SQUID chamber, after which the desolvated samples from **1**·2C_2Cl_4 were measured over a temperature cycle of 300–2–300 K. The magnetic properties of **1**·2.5CH_3OH were evaluated with a temperature cycle of 300–2–350 K while immersed in a small amount of CH_3OH solution. The magnetic chamber was subsequently heated to 395 K for one hour to facilitate in situ loss of the surface solvent and guest molecules, followed by a reduction to 300 K, and measurements were taken over a temperature cycle of 300–2–300 K.

Variable-temperature FTIR spectra. In situ Diffuse Reffectance Infrared Fourier Transform Spectroscopy (DRIFTS) measurements were performed using a Bruker Vertex 70 spectrometer. The samples were placed in a sample tank. During the measurement process, the crystalline powders of **1**·2C_2Cl_4 were heated under N_2 flow (10 mL min^{-1}) from 293 to 503K for 2 hours, and the data were collected within the temperature range of 350–503 K. The crystalline powders of **1**·2.5CH_3OH underwent heating under N_2 flow (10 mL min^{-1}) from 293 to 423K for 1.5 hours, and the data were acquired within the temperature range of 310–423 K.

Thermogravimetric (TGA) Analyses. TGA measurements were recorded under a nitrogen flow (20 mL min^{-1}) on a NETZSCH TG 209 thermobalance in a temperature range of 20−600°C with rates of 5°C min^{-1} from 20 to 200°C, 10°C min^{-1} from 200 to 400°C, and 20°C min^{-1} from 400 to 600°C.

Pure Gas Adsorption Tests. The nitrogen adsorption isotherms and pore size distribution were determined using a Kubo-X1000 Analyzer. Gas sorption isotherms were conducted on a Micromeritics (3FLEX) apparatus. Prior to gas measurement, the **1**·2.5CH_3OH samples were subjected to degassing at 100°C under dynamic vacuum conditions for 2 hours to ensure complete activation.

Dynamic Breakthrough Tests. Breakthrough experiments were carried out using a custom-made dynamic gas breakthrough apparatus. A stainless steel column (4.6 mm inner diameter × 50 mm), filled with 0.4242 g of fully activated sample, was employed for the experiments. The flow rate of the gas through the system was controlled by a mass flow controller. The effluent gas from the column was monitored at 30-second intervals using gas chromatography (Agilent 7890B) equipped with a thermal conductivity detector (TCD). Following each separation experiment, the sample was regenerated through heating at 50°C under vacuum for 30 minutes.

IAST adsorption selectivity calculation: The experimental isotherm data for pure C_2H_2, C_2H_4, and CH_4 (measured at 273 K) were fitted using a Langmuir-Freundlich (L-F) model:

$$q = \frac{a * b * p^c}{1 + b * P^c}$$

Where q and p are adsorbed amounts and pressures of component i, respectively.

Using the pure component isotherm fits, the adsorption selectivity is defined by

$$S_{ads} = \frac{q_1 / q_2}{p_1 / p_2}$$

Where q_i is the amount of i adsorbed and p_i is the partial pressure of i in the mixture.

We used the following written codes to simulate the adsorption selectivity of C_2H_2/CO_2 in **Fig. 6**:

28 # No. of Pressure Point

y1, y2 # Molar fraction of binary mixture (y1 and y2, y1 + y2 = 1)

1, 2, 3, 4, 5, 6, 7, 8, 9, 10, 20, 30, 40, 50, 60, 70, 80, 90, 100, 101, 102, 103, 104, 105, 106, 107, 108, 109 #The unit is same parameter b, kPa

a1, a2 # fitting parameter Nsat (A1) for both component (Unit: mmol/g)

b1, b2 # fitting parameter b1 for both components (Unit: kPa^{-1})

c1, c2 # fitting parameter c1 for both components

0, 0 # fitting parameter Nsat2(A2) for both component(Unit: mmol/g)

0, 0 # fitting parameter b2 for both components (Unit: kPa^{-1})

1, 1 # fitting parameter c2 for both components

Standardization of the C−H and B−H bond lengths. The $C_6NH_5{\cdot\cdot}^{NCBH_3^-}$ portion with normalised C–H (1.09 Å) and B–H (1.21 Å) bonds were modelled with AutoCAD software. The coordinates of the hydrogen atom were obtained by the model and hydrogen atoms were generated by Material studios.

Computational Details. The Young's modulus (*E*) of the desolvated state **1** was calculated using the Cambridge Serial Total Energy Package (CASTEP) module within Materials Studio. This computational method employs Density Functional Theory (DFT) to predict material properties at the atomic scale. The flexibility matrix (S) was computed utilizing CASTEP, and the resulting data were used to illustrate the anisotropy of Young's modulus in three dimensions via MATLAB software[2].

All Gas adsorption simulations were performed using the Sorption model, within the Compass III force field. The electrostatic and van der Waals were Ewald and Atom based respectively. The adsorption process was simulated at 298 K and 1 bar. The generalized gradient approximation (GGA) method with Perdew-Burke-Ernzerhof (PBE) function was employed to describe the interactions between core and electrons. The force and energy convergence criterion were set to 0.002 Ha $Å^{-1}$ and 10^{-5} Ha, respectively. The elastic constants were calculated via CASTEP model with energy cutoff of 380 eV.

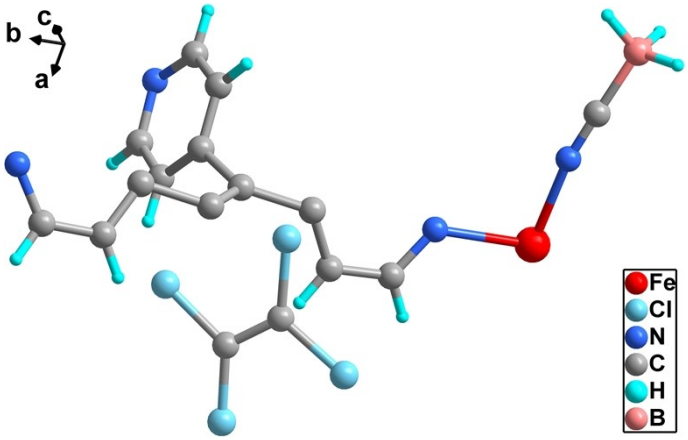

Figure S1. The asymmetric unit of **1**·$2C_2Cl_4$.

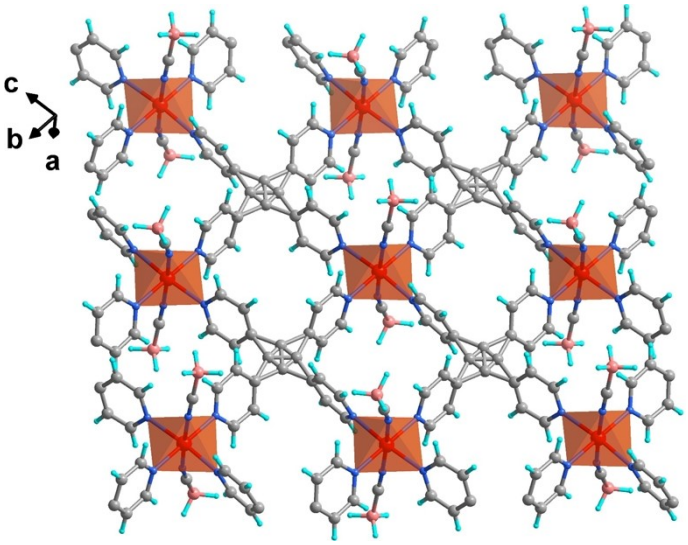

Figure S2. The Coordination mode of Fe^{2+} ions in **1**·$2C_2Cl_4$.

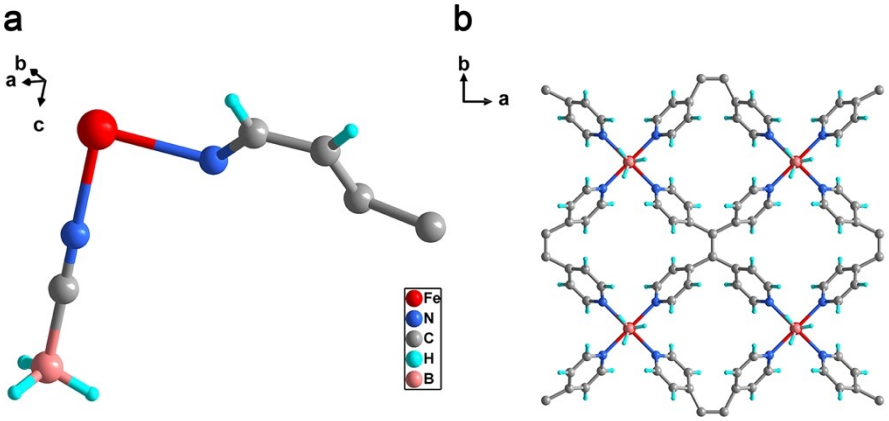

Figure S3. The asymmetric unit (**a**) and the 2D layer structure (**b**) of the partially desolvated state by **1**·$2.5CH_3OH$.

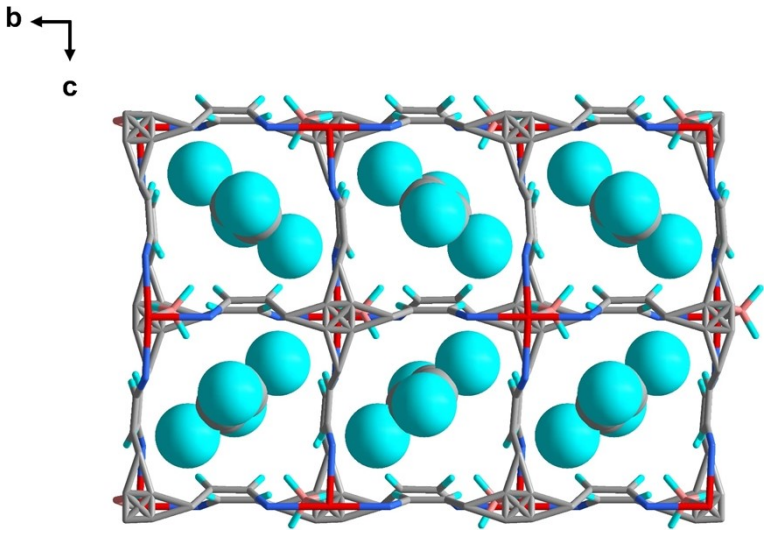

Figure S4. The arrangement of C_2Cl_4 molecules in adjacent layers of **1**·2C_2Cl_4.

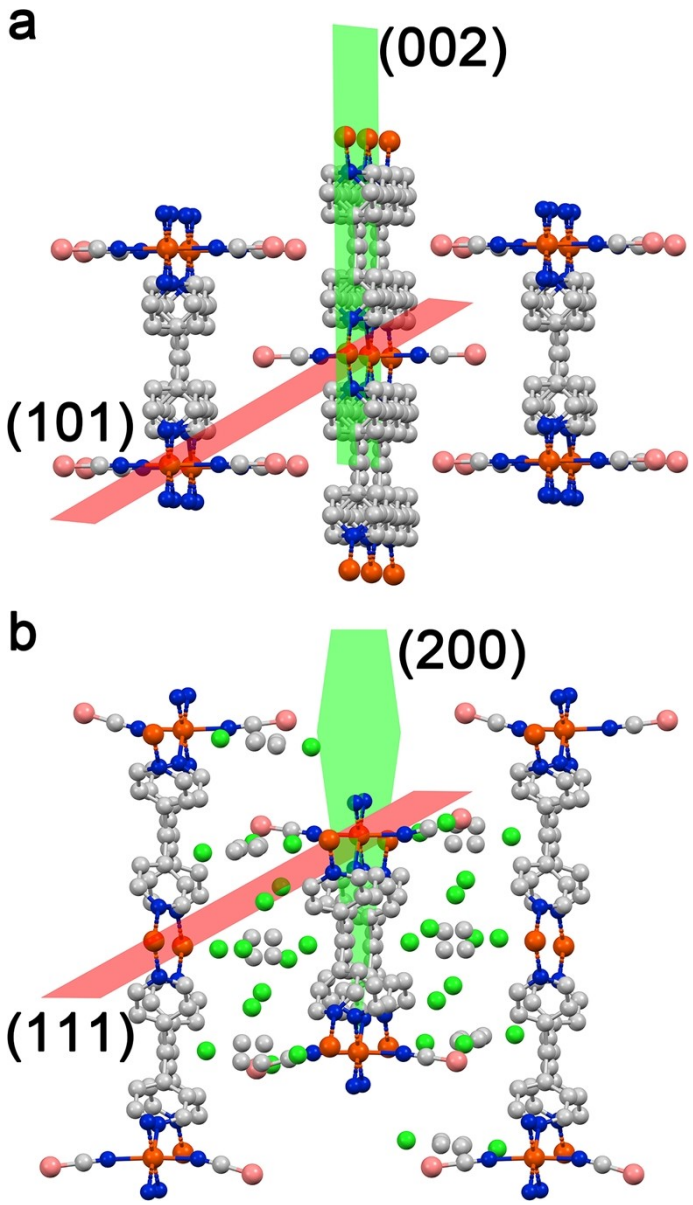

Figure S5. The selected planes in the crystal structure. **a** The (002) and (101) planes of the desolvated state **1**. **b** The (200) and (111) planes of **1**·$2C_2Cl_4$.

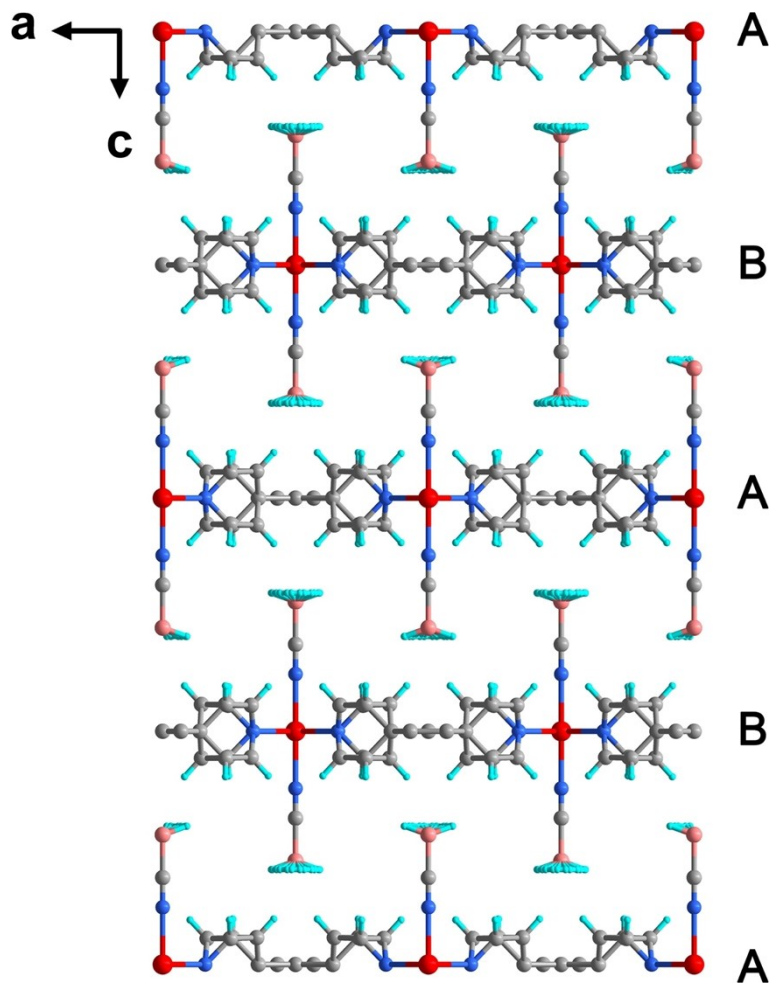

Figure S6. The ABAB-stacked structure of **1.**

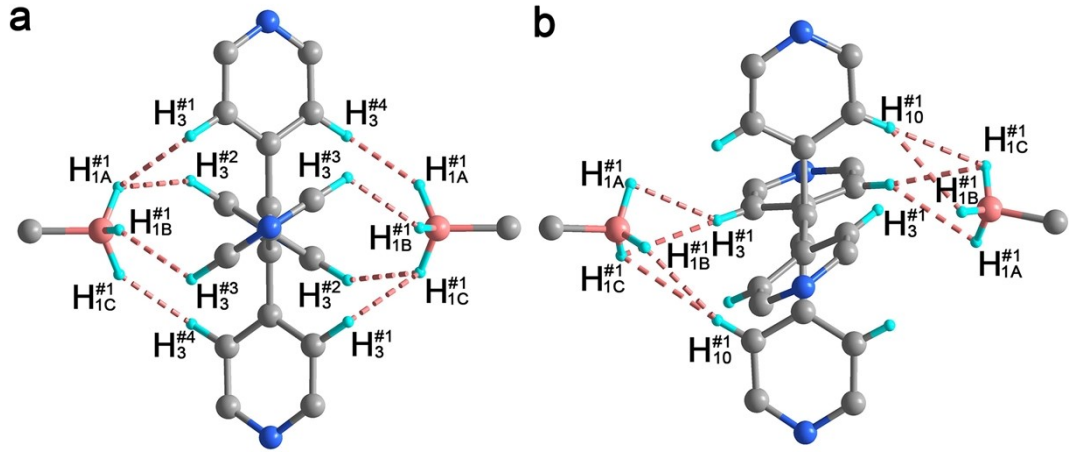

Figure S7. The C−H$^{\delta+}$···H$^{\delta-}$−B dihydrogen bonds of **1** (**a**) and **1**·2C_2Cl_4 (**b**).

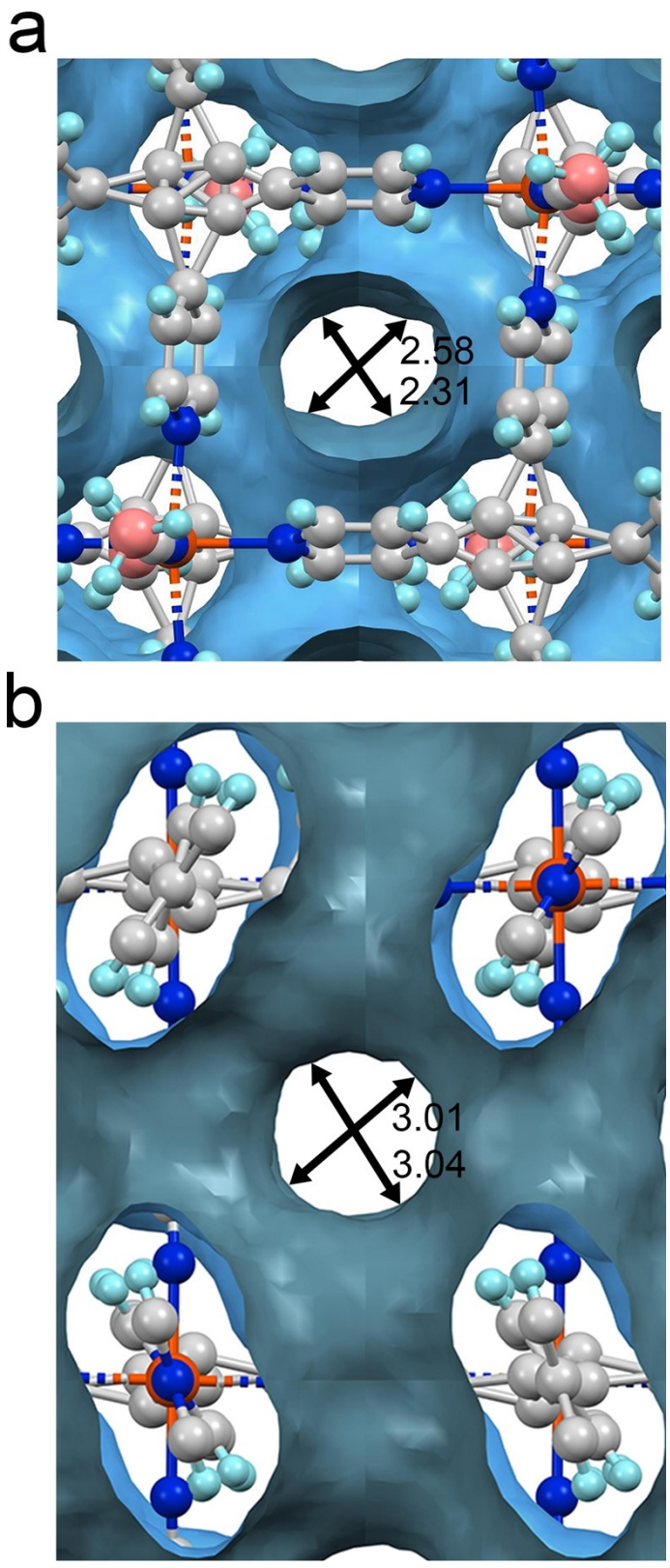

Figure S8. The circular windows of 1·2C_2Cl_4 along two directions. Calculations performed with PLATON indicate that the accessible voids in the compound **1**·2C_2Cl_4 after removal of C_2Cl_4 molecules constitutes about 44.4% per cent unit cell. The cavity deformation and increased capacity suggest that the C_2Cl_4 guest molecules exert an expansive effect on the framework of **1**.

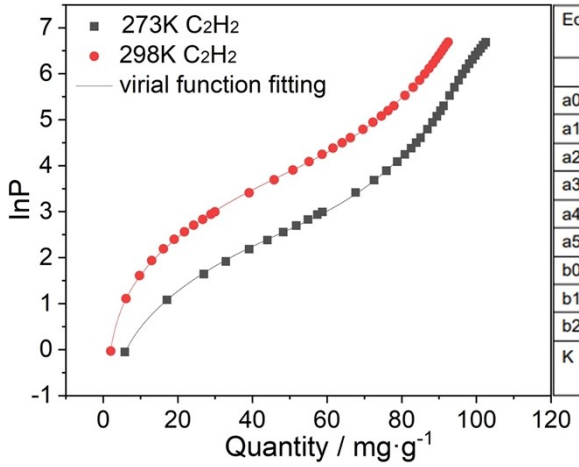

Eqtation	ln(x)+1/K*(a0+a1*x+a2*x^2+a3*x^3+a4*x^4+a5*x^5) +(b0+b1*x+b2*x^2)	
	Value	Standard Error
a0*	-3533.1038	127.20748
a1*	-20.20468	5.95885
a2*	0.50699	0.13268
a3*	-0.01155	0.00264
a4*	1.2096E-4	2.69251E-5
a5*	-3.85364E-7	9.97686E-8
b0*	11.18062	0.43252
b1*	0.05414	0.01812
b2*	-8.8781E-5	1.64206E-4
K	273	0
	298	0

Figure S9. C_2H_2 fit isotherms of **1** at 273 K and 298 K by virial equation.

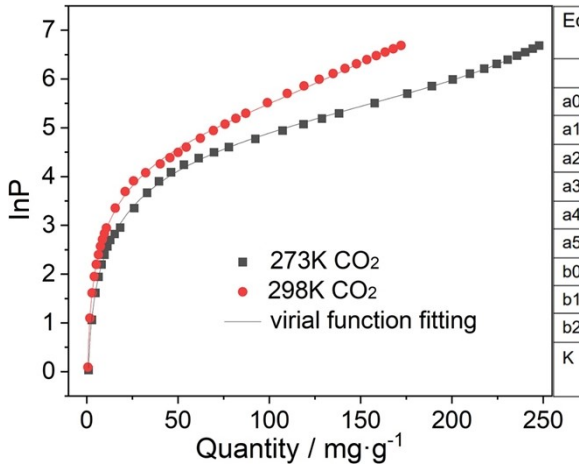

Eqtation	ln(x)+1/K*(a0+a1*x+a2*x^2+a3*x^3+a4*x^4+a5*x^5) +(b0+b1*x+b2*x^2)	
	Value	Standard Error
a0*	-1523.20978	61.91242
a1*	6.48467	2.12037
a2*	-0.12614	0.01684
a3*	2.60201E-4	1.59192E-4
a4*	-1.04792E-6	7.45408E-7
a5*	1.73244E-9	1.22982E-9
b0*	5.60637	0.21568
b1*	-0.01693	0.00739
b2*	3.56336E-4	4.39665E-5
K	273	0
	298	0

Figure S10. CO_2 fit isotherms of **1** at 273 K and 298 K by virial equation.

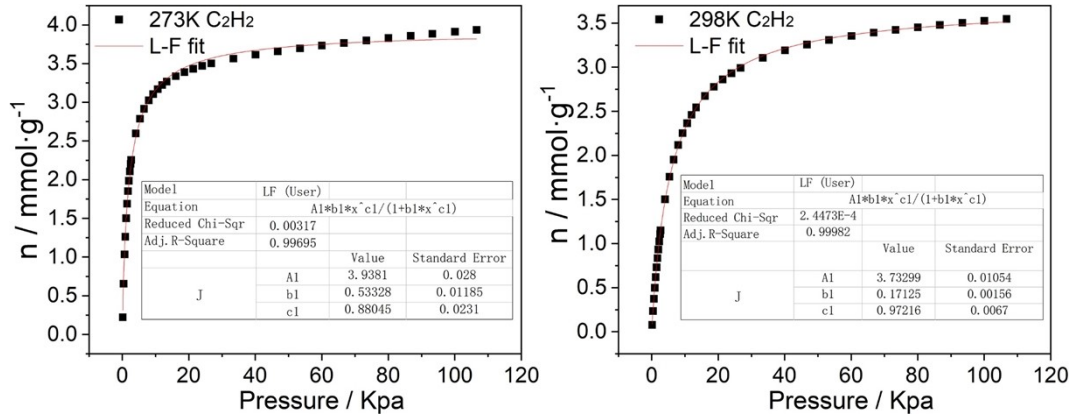

Figure S11. C_2H_2 fit isotherm of **1** at 273 and 298 K by L-F model.

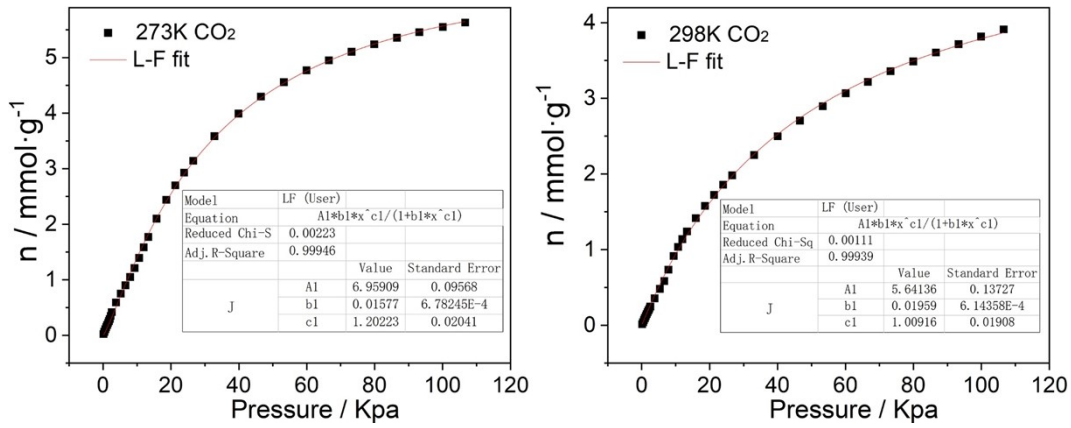

Figure S12. CO_2 fit isotherm of **1** at 273 and 298 K by L-F model.

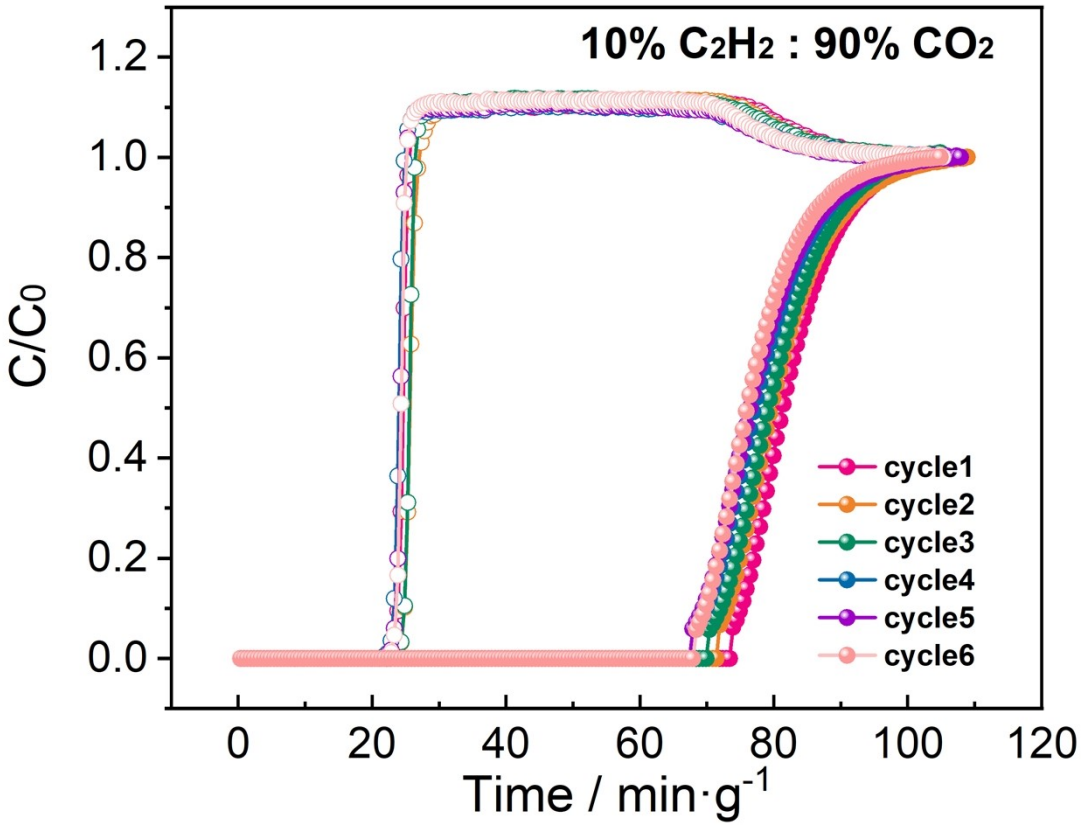

Figure S13. The cyclic breakthrough curves for 1/9 binary C_2H_2/CO_2. The breakthrough experiment cyclability (6 times) for the C_2H_2/CO_2 (1/9, v/v) mixture with a gas flow rate of 2 mL min^{-1} at 298 K.

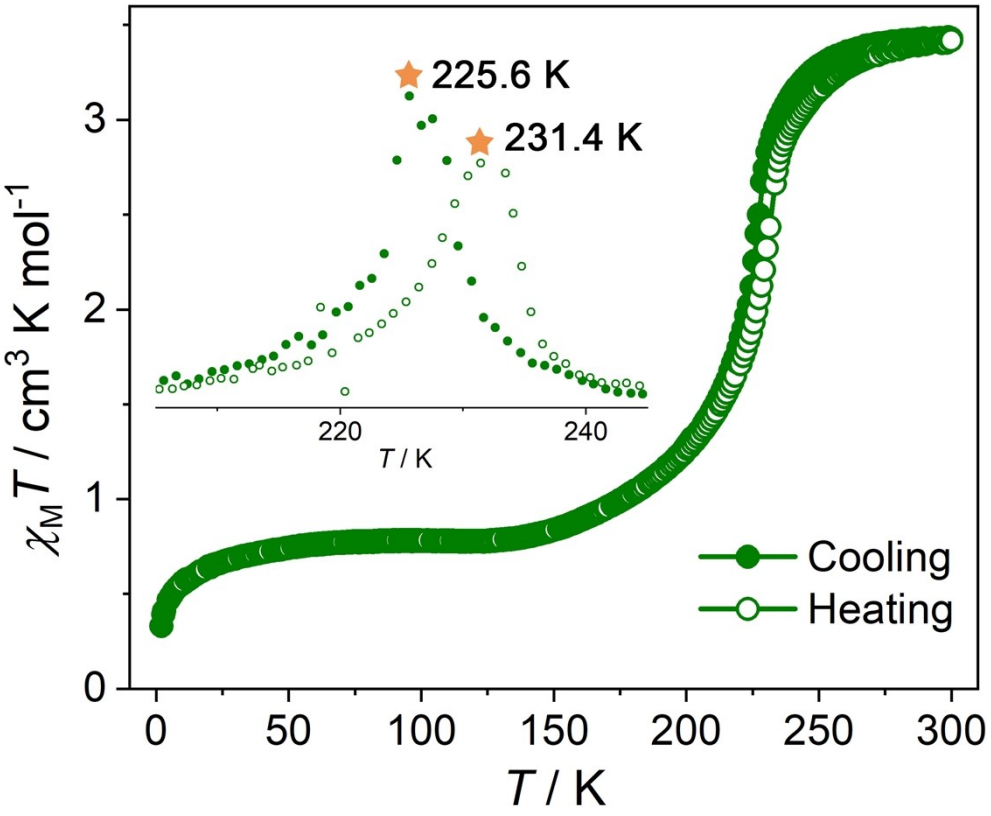

Figure S14. Thermal hysteresis loop of 5.8 K for **1**. (inset: derivative of $\chi_M T$ versus T curve)

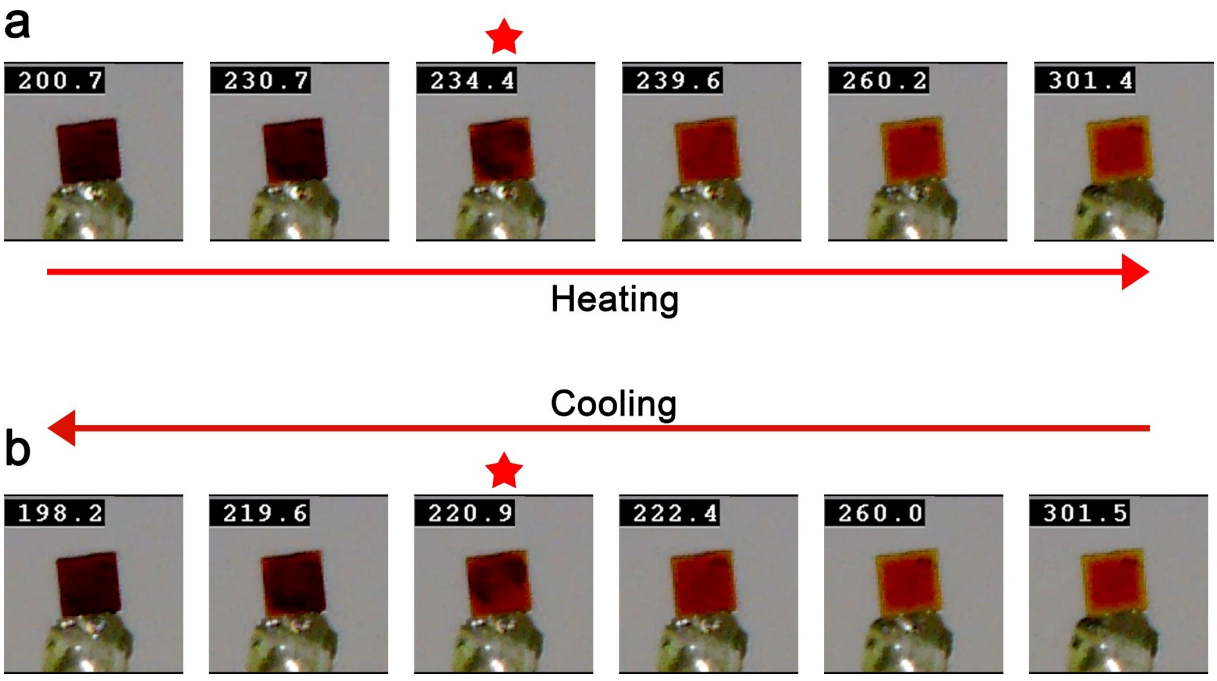

Figure S15. The slight thermal hysteresis loop that showed in photographs of the free crystal during the two cycles of heating and cooling in video 2.

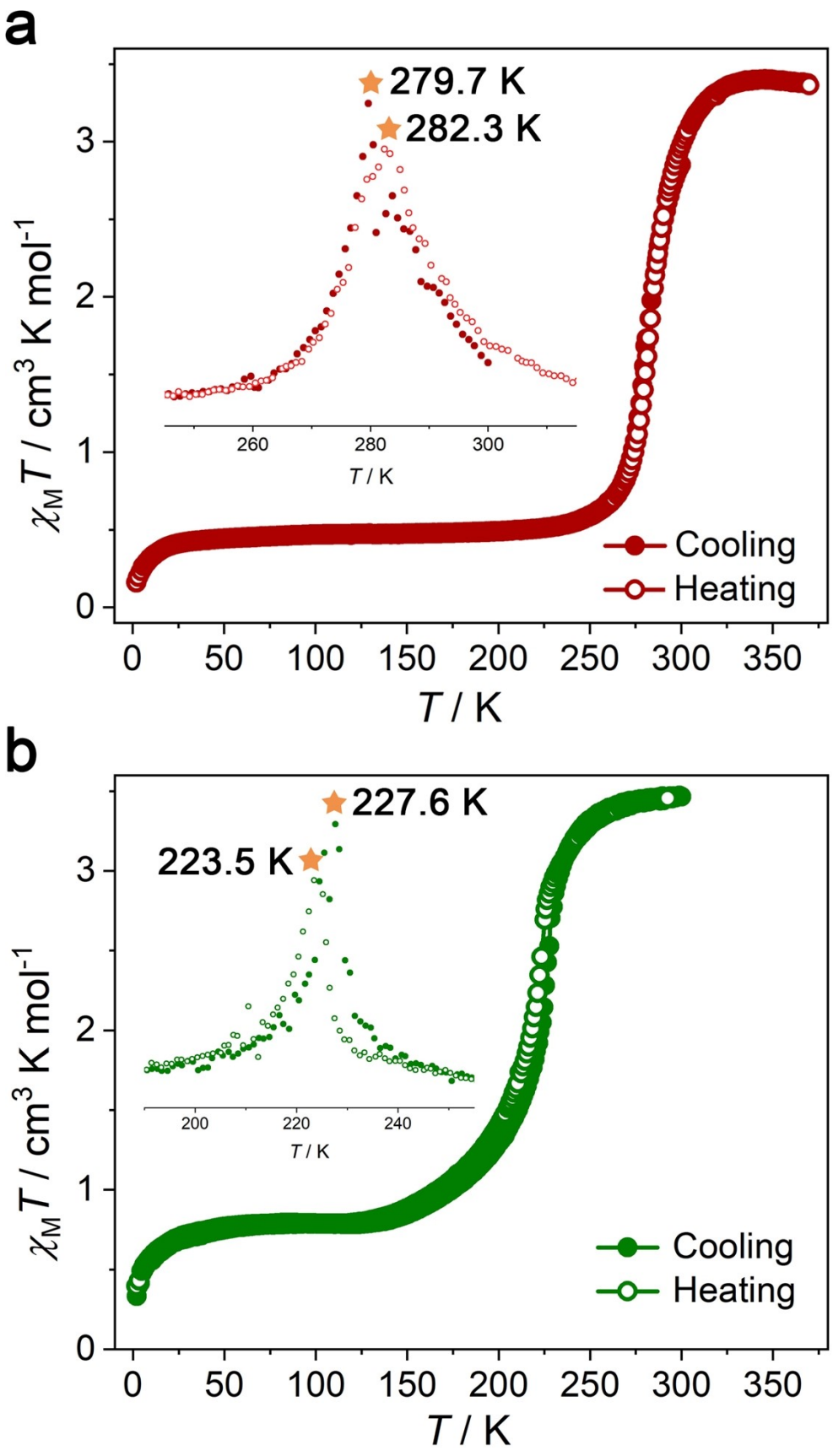

Figure S16. Thermal hysteresis loop of 2.6 K for **1**·2.5CH_3OH and of 4.1 K for **1**. (inset: derivative of $\chi_M T$ versus T curve).

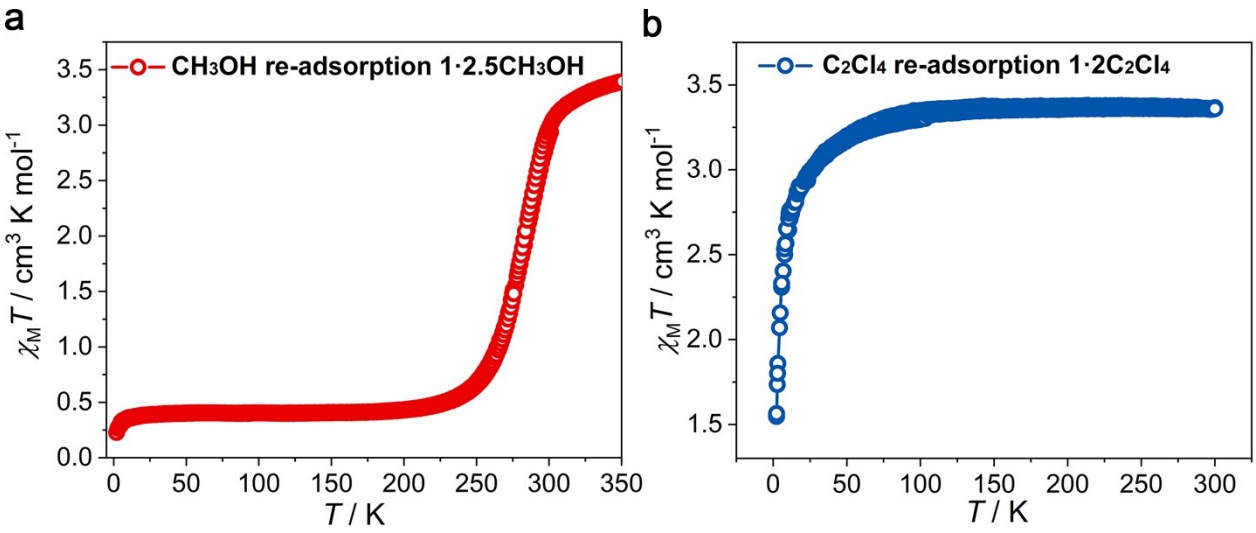

Figure S17. Temperature-dependence of the $\chi_M T$ values of CH_3OH (**a**) and C_2Cl_4 (**b**) re-adsorption samples.

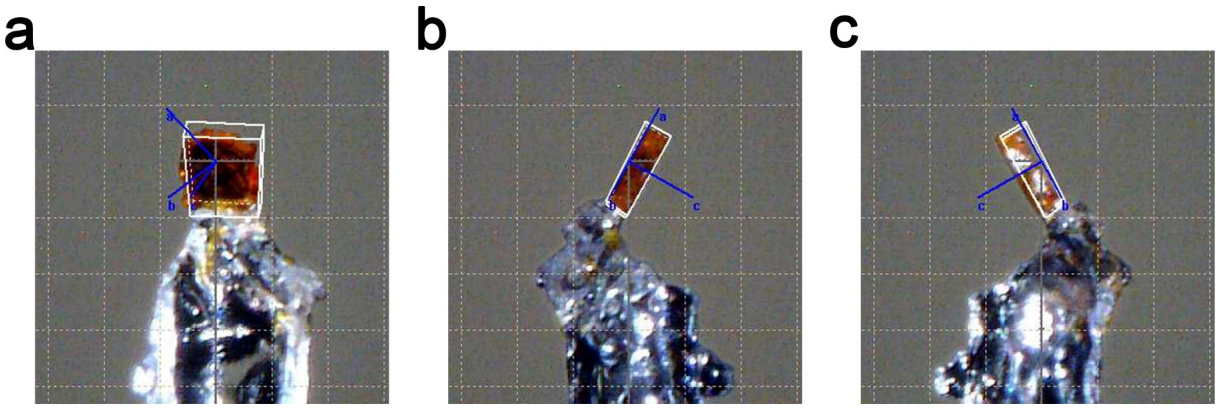

Figure S18. The face index of single crystal of the partially desolvated state by **1**·2.5CH_3OH.

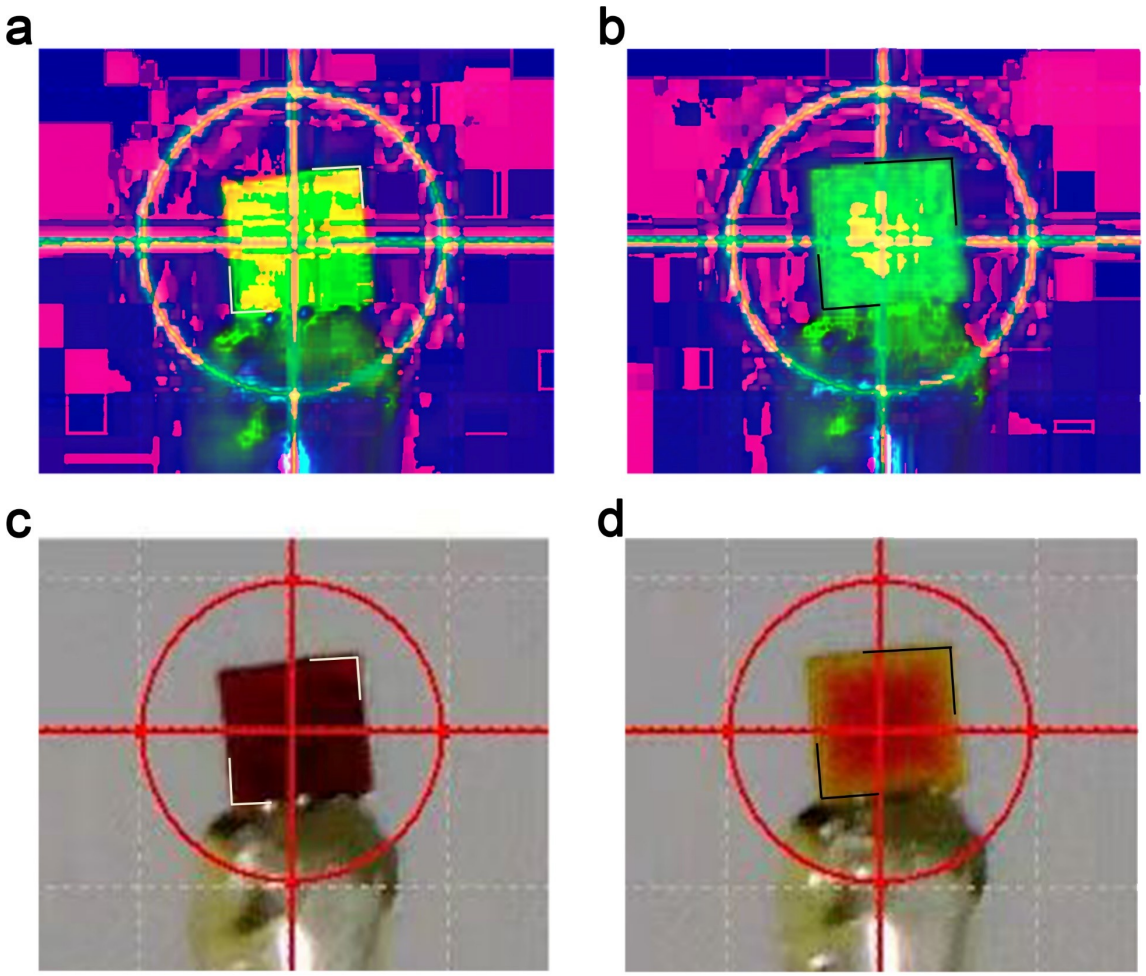

Figure S19. The rule for dimensioning the free crystal. The photograph converted by HSB filter for the free crystal of the partially desolvated state by **1**·2.5CH_3OH at 198 (**a**) and 301 K (**b**). The original photograph for the free crystal at 198 (**c**) and 301 K (**d**).

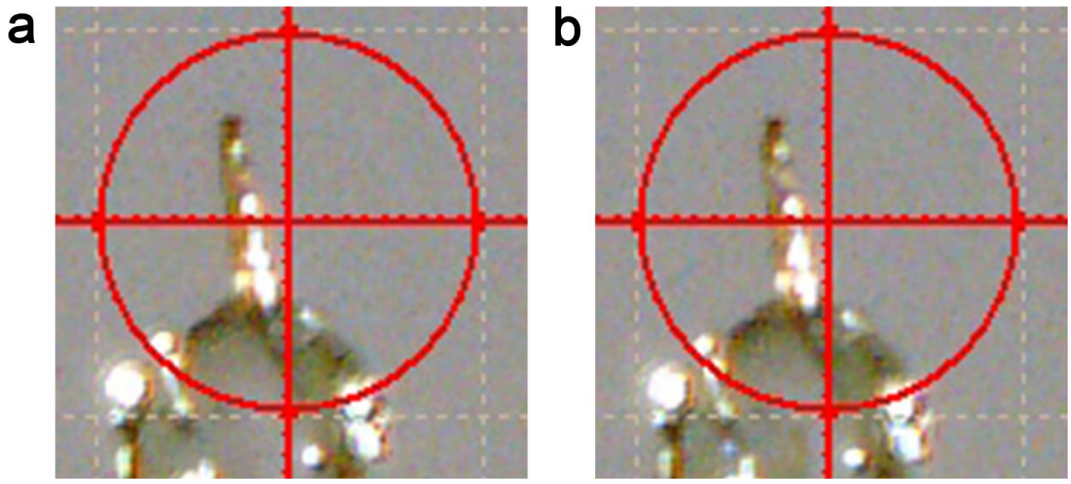

Figure S20. The side-view photograph of the free crystal before (**a**) and after (**b**) undergoing two cycles of heating and cooling.

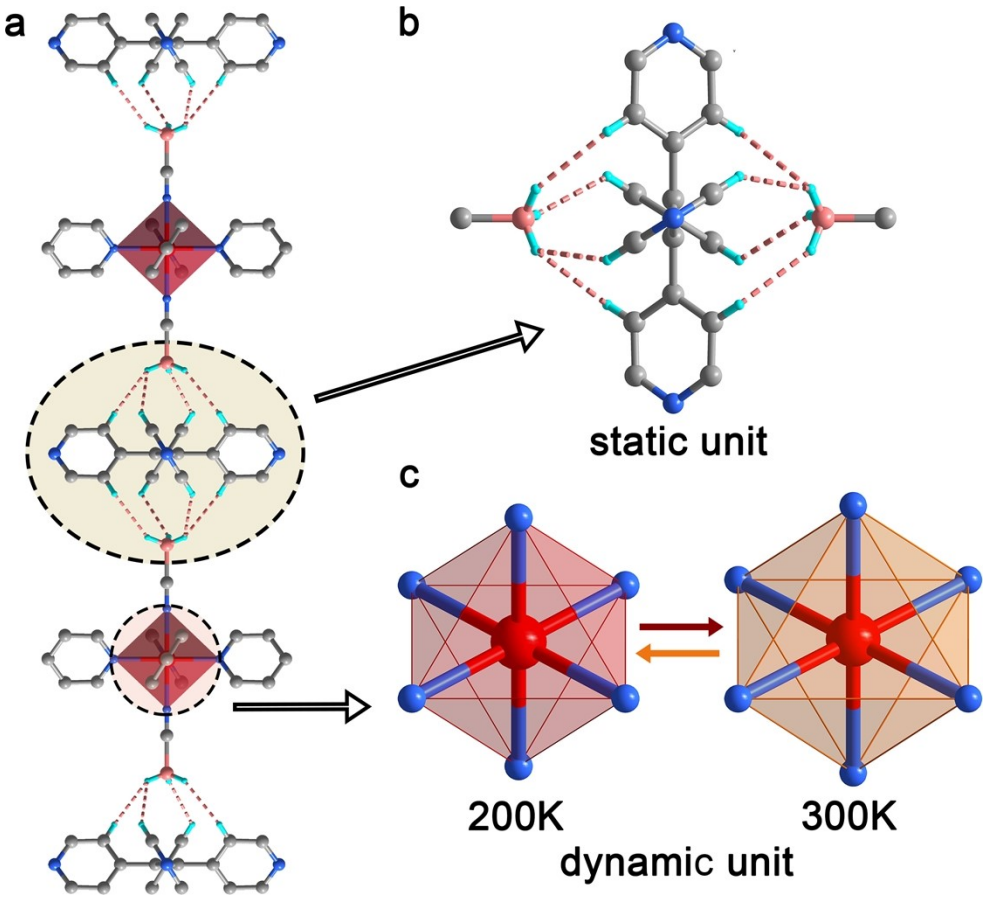

Figure S21. The static and dynamic units of the partially desolvated state by **1**·2.5CH_3OH upon macroscopic shape change in the free crystal. The 2D layers stacked in ABAB mode are stabilized by pillared multiple C−$H^{\delta+}\cdots H^{\delta-}$−B DHBs to form the 3D supramolecular structure (**a**), with the tpe ligand bound by DHBs serving as a static unit (**b**) and the SCO behavior of the linked Fe^{2+} metal center acting as adynamic unit (**c**).

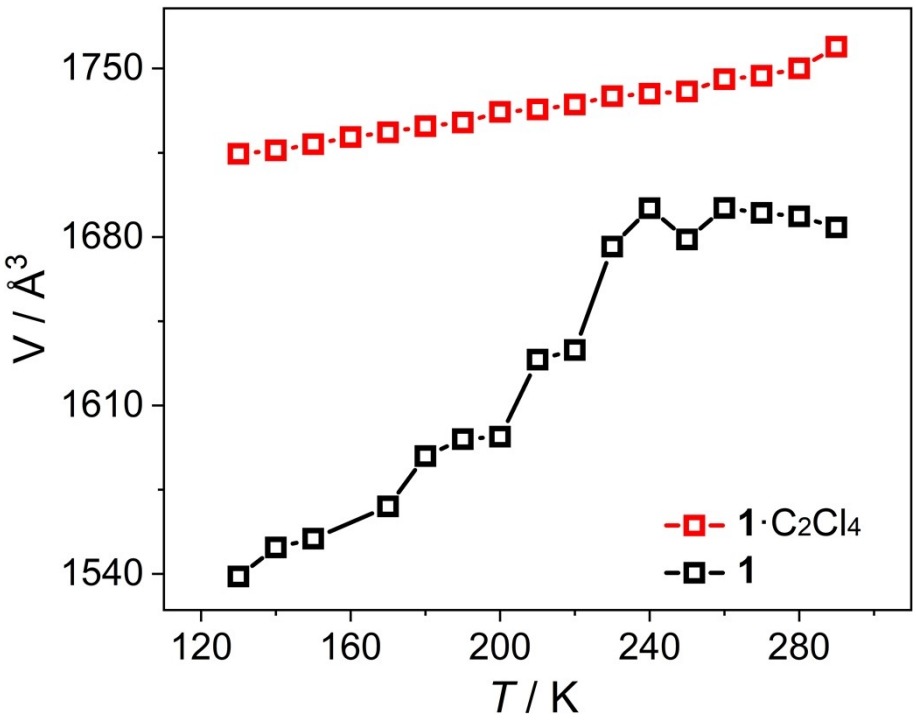

Figure S22. The comparison of temperature-dependent unit-cell volume in **1**·2C_2Cl_4 and 1.

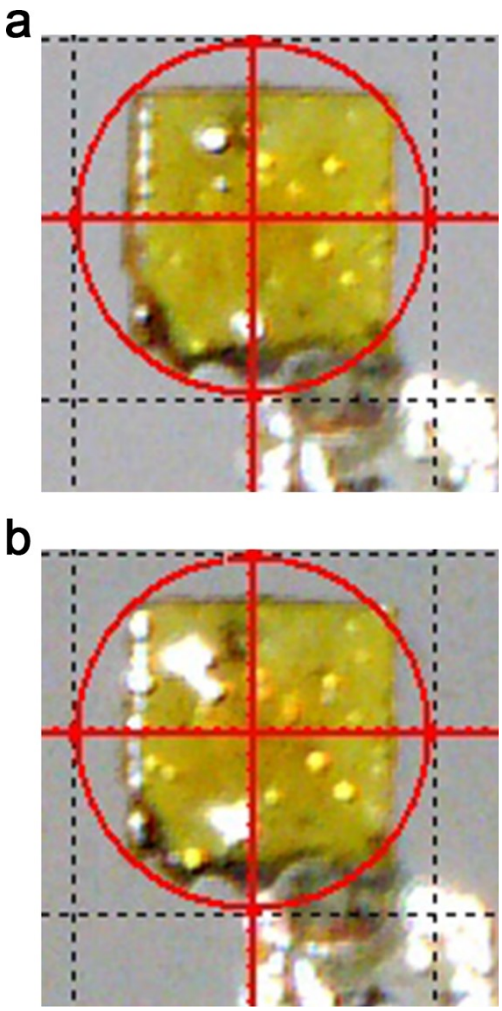

Figure S23. The photograph for the free crystal of **1**·2C_2Cl_4 at 200 (**a**) and 300 K (**b**). The free crystal of **1**·2C_2Cl_4 at 200 K was observed to slightly shift downwards, likely due to the shrinkage of rubber cement used for fixing the glass wire under the low temperature gas flow. Upon comparing the sizes of the crystal shapes, it was determined that the effect of conventional thermal expansion on the macroscopic shape is very small.

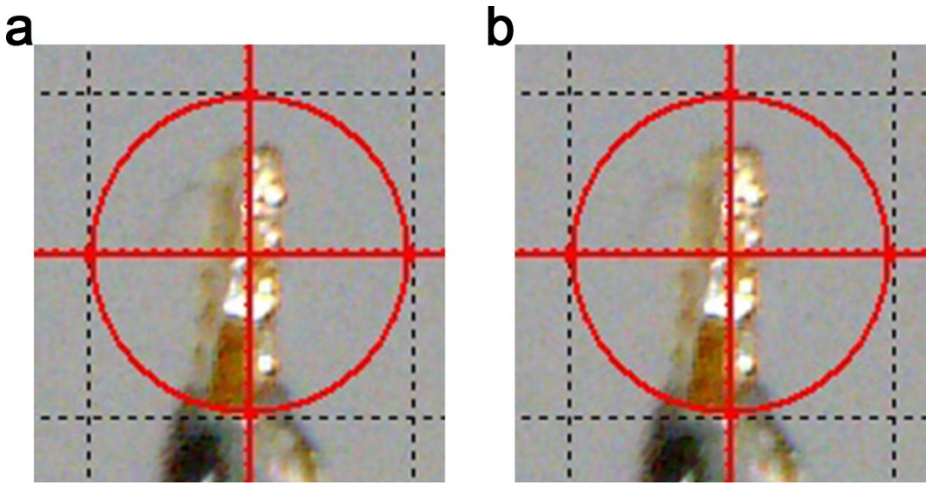

Figure S24. The side-view photograph of the free crystal of **1**·2C_2Cl_4 before (**a**) and after (**b**) undergoing two cycles of heating and cooling.

Table S1. Crystal data and structural refinements for **1**·2C_2Cl_4.

	1·2C_2Cl_4		
Temperature/K	200	448(desolvation)	298(desolvation)
Formula	$C_{28}H_{22}B_2Cl_8FeN_6$	$C_{24}H_{22}B_2FeN_6$	
Mr/g mol^{-1}	803.58	471.94	
Crystal size/mm	0.15×0.15×0.05	0.07×0.07×0.02	
Wavelength/Å	0.71073	0.71073	
Space group	*Pbcn*	*I*4/mmm	*I*4/mmm
Crystal color	yellow	yellow	yellow
Crystal system	orthorhombic	tetragonal	tetragonal
a/Å	17.9178(8)	9.856(3)	9.8528(18)
b/Å	13.9608(6)	9.856(3)	9.8528(18)
c/Å	13.9443(10)	17.199(8)	17.332(6)
α/°	90	90	90
β/°	90	90	90
γ/°	90	90	90
Volume/Å^3	3488.1(3)	1670.8(13)	1682.6(9)
Z	4	2	2
D_c / g cm^{-3}	1.530	0.938	0.932
μ / mm^{-1}	1.076	0.468	0.465
F(000)	1616.0	488.0	488.0
*θ*range/°	3.456 to 29.227	2.382 to 24.994	2.378 to 26.452
Data/restraints/parameters	4291/0/235	460/69/42	542/13/42
Goodness-of-fit on F^2	1.052	2.467	1.101
Reflections collected	20307	3842	4743
R_1 [I ≥ 2σ(I)]	0.0487	0.3234	0.0850
wR_2 [all data]	0.1281	0.6124	0.2437
Largest diff. peak and hole/e.Å^{-3}	0.73/-0.45	4.44/-1.93	1.37/-0.96

Table S2. Crystal data and structural refinements for the partially desolvated state by **1**·2.5CH_3OH.

The partially desolvated state by 1·2.5CH_3OH		
Temperature/K	200	301
Formula	$C_{24}H_{22}B_2FeN_6$	
M_r/g mol^{-1}	471.94	
Crystal size/mm	0.1×0.1×0.05	
Wavelength/Å	0.71073	
Space group	*I*4/mmm	*I*4/mmm
Crystal color	red	yellow
Crystal system	tetragonal	tetragonal
a/Å	9.5534(5)	9.8237(5)
b/Å	9.5534(5)	9.8237(5)
c/Å	16.771(3)	17.274(2)
α/°	90	90
β/°	90	90
γ/°	90	90
Volume/Å^3	1530.6(3)	1667.0(3)
Z	2	2
D_c / g cm^{-3}	1.037	0.940
μ / mm^{-1}	0.511	0.469
F(000)	500.0	488.0
*θ*range/°	3.873 to 29.013	3.764 to 29.064
Data/restraints/parameters	580/0/42	639/6/42
Goodness-of-fit on F^2	1.174	1.086
Reflections collected	3489	5015
R_1 [$I \geq 2\sigma(I)$]	0.0417	0.0462
wR_2 [all data]	0.1151	0.1262
Largest diff. peak and hole/e.Å^{-3}	0.78/-0.36	0.32/-0.38

Table S3. The experimental values for selected distances and angles of C−H$^{\delta+}$···H$^{\delta-}$−B DHBs interactions of **1**·2C_2Cl_4 at 200 K.

entry	C−H···H−B	H···H (Å)	C−H···H (º)	H···H−B (º)
1	C#1 3−H#1 3···H#1 1A−B#1	2.3027(3)	137.309(4)	86.204(5)
2	C#1 3−H#1 3···H#1 1C−B#1	2.2231(1)	163.911(3)	89.902(2)
3	C#1 10−H#2 10···H#1 1B−B#1	2.3695(2)	142.726(4)	106.257(4)
4	C#1 10−H#2 10···H#1 1C−B#1	2.5683(2)	168.054(2)	95.762(1)
5	C#2 10−H#2 10···H#2 1C−B#2	2.5683(2)	168.054(2)	95.762(2)
6	C#2 10−H#2 10···H#2 1B−B#2	2.3695(4)	142.726(3)	106.257(3)
7	C#2 3−H#1 3···H#2 1C−B#2	2.2231(1)	163.911(1)	89.902(1)
8	C#2 3−H#1 3···H#2 1A−B#2	2.3027(4)	137.309(6)	86.204(2)

Table S4. The experimental values for selected distances and angles of C−H$^{\delta+}$···H$^{\delta-}$−B DHBs interactions of the desolventized state·from **1**·2C_2Cl_4 at 298 K.

entry	C−H···H−B	H···H (Å)	C−H···H (º)	H···H−B (º)
1	C#1 3−H#1 3···H#1 1A−B#1	2.6326(5)	111.50(2)	105.363(1)
2	C#2 3−H#2 3···H#1 1A−B#1	2.2859(7)	146.58(1)	127.835(2)
3	C#3 2−H#3 3···H#1 1B−B#1	2.2413(1)	123.54(4)	131.505(3)
4	C#4 3−H#4 3···H#1 1C−B#1	2.0895(2)	135.549(1)	147.243(1)
5	C#4 3−H#4 3···H#2 1A−B#2	2.0895(5)	135.549(2)	147.243(2)
6	C#3 2−H#3 3···H#2 1B−B#2	2.2413(1)	123.54(1)	131.505(3)
7	C#2 3−H#2 3···H#2 1C−B#2	2.2859(7)	146.58(1)	127.835(2)
8	C#1 3−H#1 3···H#2 1C−B#2	2.6326(3)	111.50(2)	105.363(1)

Table S5. Single-crystal elastic stiffness constants (C_{ij}'s) of **1**. The tetragonal crystal symmetry entails 6 independent elastic coefficients.

Structure	C_{11}	C_{12}	C_{13}	C_{33}	C_{44}	C_{66}
1	13.6	-33.969	-45.2365	-59.905	3.69067	31.6045

Table S6. Selected bond lengths and angles for **1**·2C_2Cl_4 at 200 K.

Fe1−N1	2.125(1)
Fe1−N2	2.212(3)
Fe1−N3	2.245(2)
Fe1−N4	2.258(3)
N1−Fe1−N2	92.34(5)
N1−Fe1−N3	90.75(7)
N1−Fe1−N3$^{\#1}$	89.48(7)
N1−Fe1−N4	87.66(5)
N2−Fe1−N3	87.15(5)
N3−Fe1−N4	92.85(5)
N1−Fe1−N1$^{\#2}$	175.31(1)
N2−Fe1−N4	180
N3−Fe1−N3$^{\#1}$	174.30(9)

Symmetry codes: #1) 1 – *x*,1 – *y*,1 – *z*; #2) 1 – *x*,+ *y*,1 / 2 – *z*.

Table S7. Selected bond lengths and angles for the desolvated state **1** by **1**·2C_2Cl_4 at different temperature,

	298 K	448 K
Fe1−N1	2.234(1)	2.13(2)
Fe1−N2	2.222(6)	2.13(2)
N1−Fe1−N2	90.0	90.0
N1−Fe1−N1$^{\#1}$	180.0	180.0
N1−Fe1−N2$^{\#1}$	90.0	90.0
N1−Fe1−N2$^{\#2}$	90.0	90.0
N1−Fe1−N2$^{\#3}$	90.0	90.0

Symmetry codes: #1) 1 – *x*,1 – *y*,1 – *z*; #2) + *y*, 1 – *x*, 1 – *z*; #3) 1 – *y*, + *x*, + *z*.

Table S8. Selected bond lengths and angles for the partially desolvated state by **1**·2.5CH_3OH at different temperature.

	200 K	301 K
Fe1−N1	1.944(4)	2.118(5)
Fe1−N2	2.006(3)	2.219(3)
N1−Fe1−N2	90.0	90.0
N1−Fe1−N1$^{\#1}$	180.0	180.0
N1−Fe1−N2$^{\#1}$	90.0	90.0
N1−Fe1−N2$^{\#2}$	90.0	90.0
N1−Fe1−N2$^{\#3}$	90.0	90.0

Symmetry codes: #1) 1 – *x*,1 – *y*,1 – *z*; #2) 1 – *y*, + *x*, + *z;* #3) + *y*, 1 – *x*, 1 – *z*.

Table S9. Selected structural parameters for **1**·C_2Cl_4, **1**, and the partially desolvated state by **1**·2.5CH_3OH at different temperatures.

Compound	**1·2C_2Cl_4**		**1**	**the partially desolvated state**	
Temperature/K	200	448	298	200	301
<Fe1−N1>[a]/Å	2.125(1)	2.13(2)	2.234(1)	1.944(4)	2.118(5)
<Fe1−N2>[a]/Å	2.240(2)	2.13(2)	2.222(6)	2.006(3)	2.219(3)
∑Fe1[b]/°	23.3	0	0	0	0
<Fe1−N−C>[c]/°	166.30(19)	180	180	180	180

[a] The average Fe–N bond lengths (Å);

[b] Octahedral distortion parameters (°);

[c] Average Fe–N–C angles within Hofmann layer.

References

[1] G. M. Sheldrick, *Acta Cryst. C*. **2015**, *71*, 3−8.

[2] J. F. Nye, Physical properties of crystals. Oxford: Clarendon Press, 1985.